nature geoscience
SUPPLEMENTARY INFORMATION
DOI: 10.1038/NGEO2931

In the format provided by the authors and unedited.

Onset and ending of the late Palaeozoic ice age triggered by tectonically paced rock weathering

Yves Goddéris[*], Yannick Donnadieu[+], Sébastien Carretier[*], Markus Aretz[*], Guillaume Dera[*], Mélina Macouin[*] and Vincent Regard[*]

[*]Géosciences Environnement Toulouse, CNRS - UPS - IRD, Toulouse, France
[+]Laboratoire des Sciences du Climat et de l'Environnement, CNRS, Gif-sur-Yvette, France

1. Additional figures referred in the main text or in the method

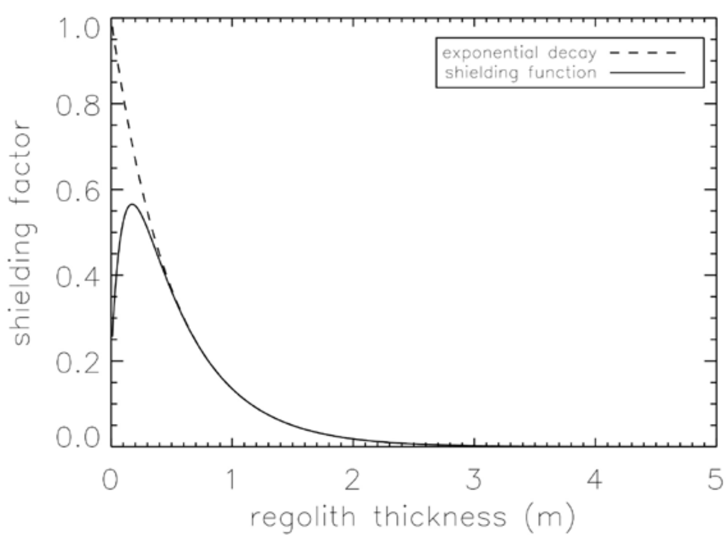

Supplementary Figure 1: The shielding factor as a function of saprolith thickness (solid line). The "humped" function behaves as an exponential decay for thick saproliths (Heimsath et al., 2009) (supply-limited weathering regime). For saprolith thinner than 20 cm, the "humped" function diverges from the exponential decay trend to simulate the transition towards a weathering-limited regime.

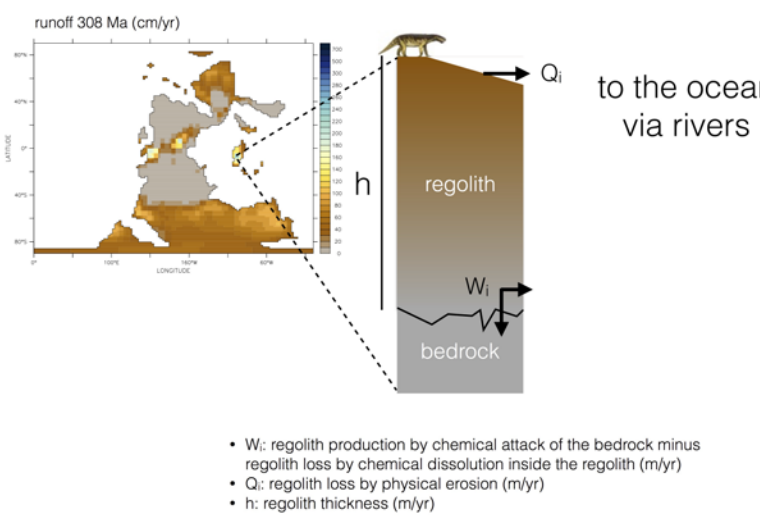

Supplementary figure 2: Schematic description of the saprolith model included in the GEOCLIM-REG simulations. W_i is the net saprolith production by chemical weathering. It is equal to the production of saprolith by chemical attack of the bedrock minus the loss by chemical weathering inside the saprolith. Q_i is the removal of saprolith by physical erosion. This mass balance is solved for each continental grid element until steady state is reached.

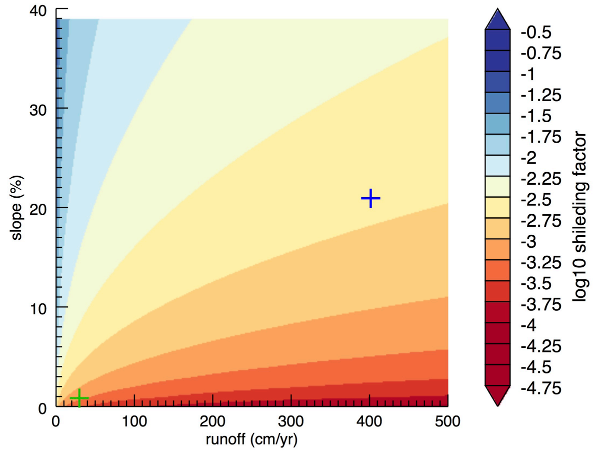

Supplementary figure 3: Log_{10} of the shielding factor calculated at steady state for a mean annual temperature of 22°C as a function of mean annual runoff and slope. The temperature is the mean annual temperature of the Rio Icacos (Puerto Rico, blue cross) and of the Nyong watershed (Cameroon, green cross). Both catchments are located in tropical humid environments, but the Rio Icacos displays steep slopes, which promote physical erosion. Consequently, the shielding factor is about one order of magnitude lower in Cameroon. Measurements predict weathering rates in the Nyong more than an order of magnitude below those in the Rio Icacos (compilation by Millot et al., 2002).

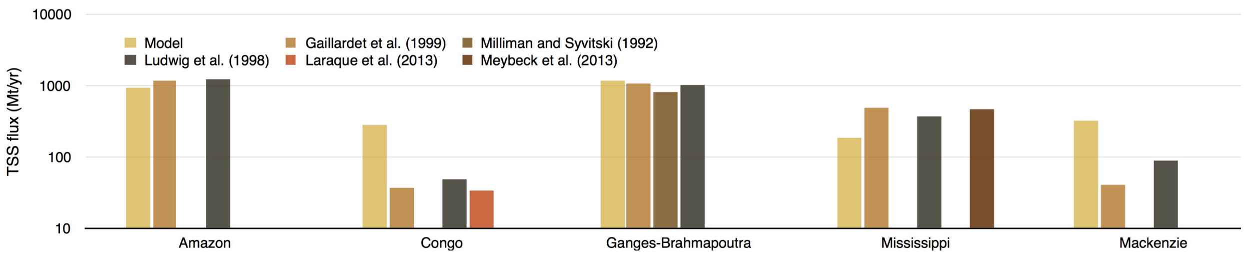

Supplementary figure 4: Present day fluxes of total suspended solid for various watersheds: comparison between the modeled flux and data (Gaillardet et al., 1999; Laraque et al., 2013; Ludwig and Probst, 1998; Meybeck et al., 2013; Milliman and Sivitski, 1992)

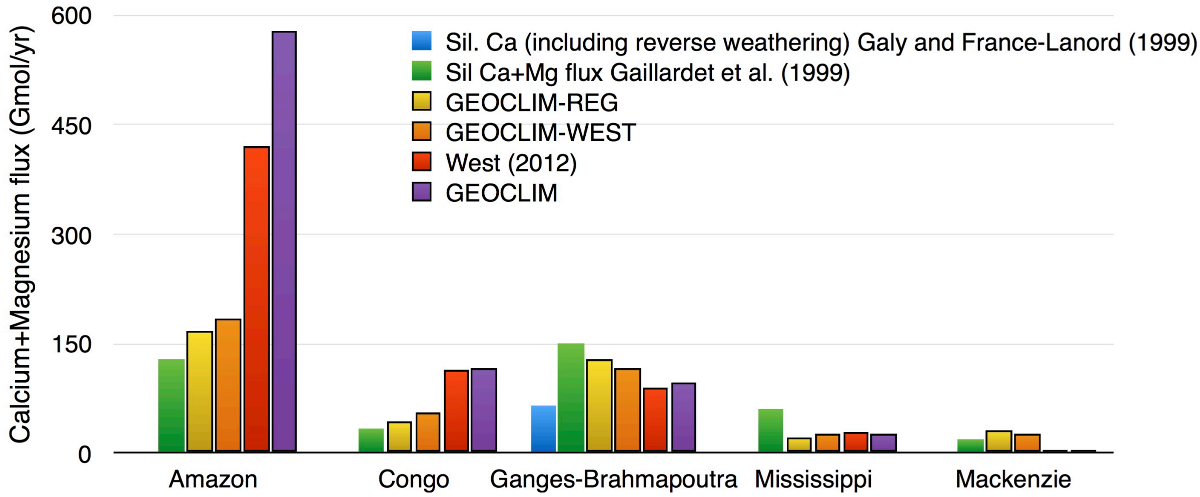

Supplementary figure 5: Present day consumption of atmospheric CO_2 by silicate rock weathering: model-data comparison (Gaillardet et al., 1999; Galy and France-Lanord, 1999). The blue and green bars stand for the data. The violet and yellow bars represent the model output respectively without and with the shielding effect. The red bars stand for the West (2012) model, with the original best fit. The orange bars stand for the West model with the set of parameters described in the Methods.

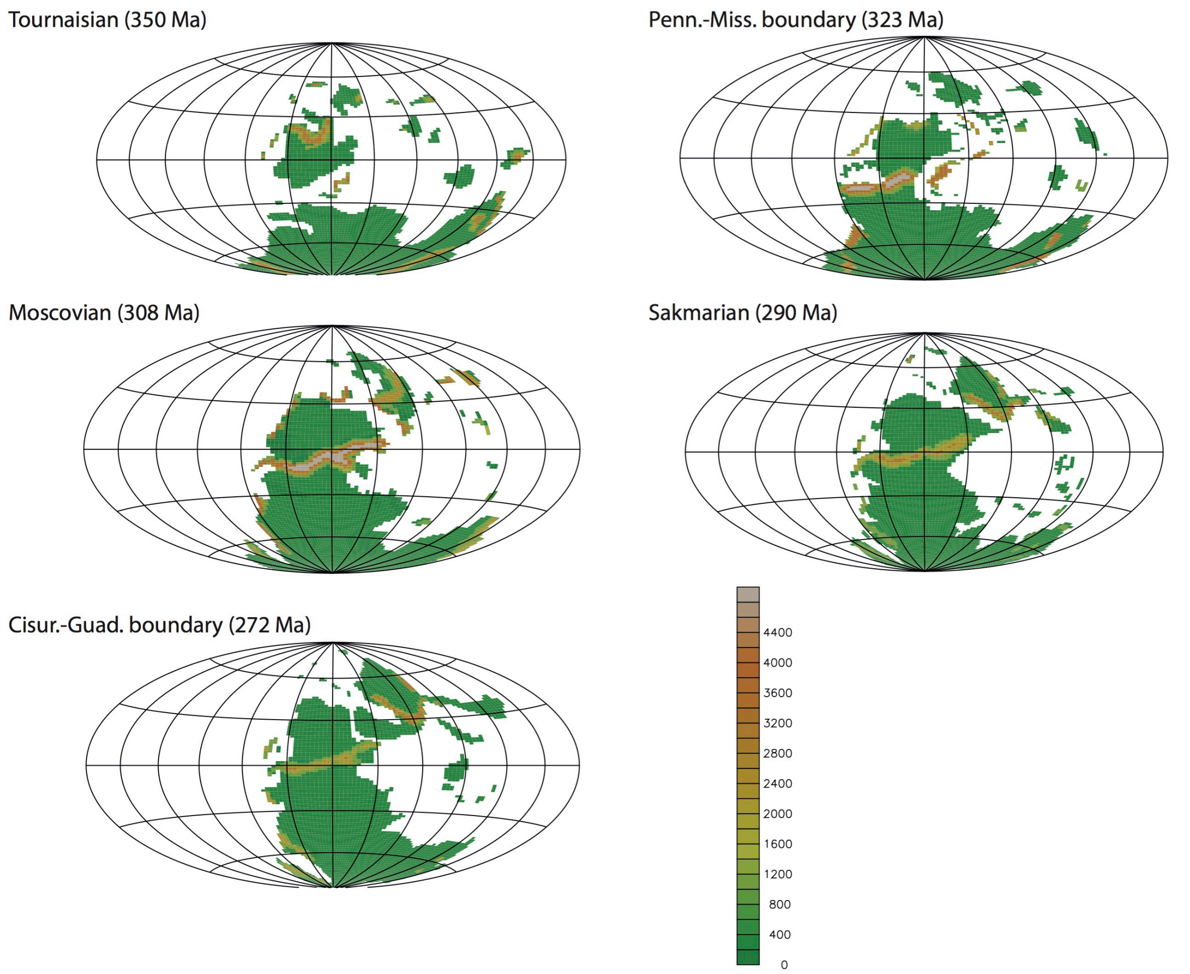

Supplementary figure 6: Paleogeographic maps of the Late Palaeozoic used in the simulations. The colored scale is the altitude (m).

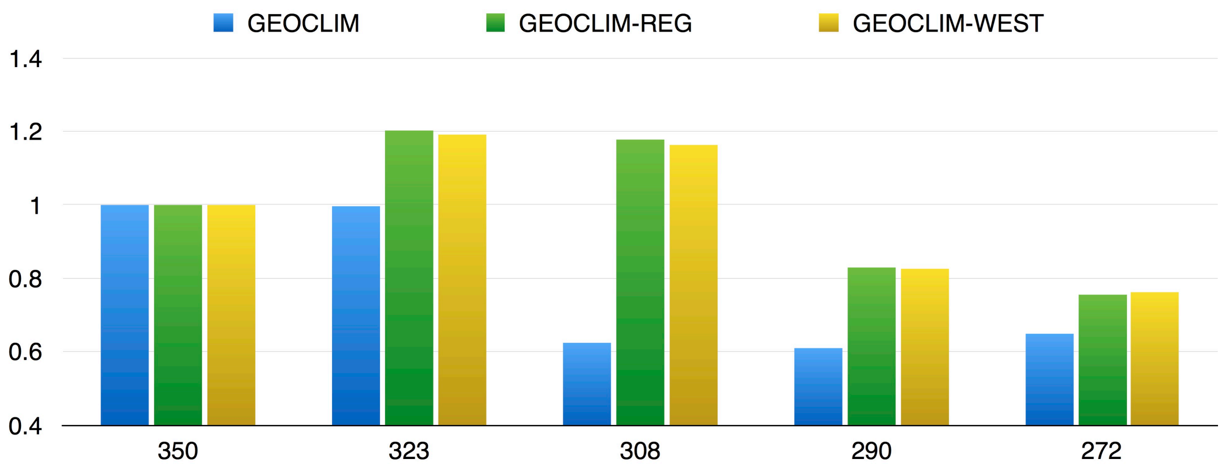

Supplementary figure 7: Consumption of CO_2 by continental silicate weathering normalized at its value at 350 Ma for each modeled time slice and for each simulation at 4 times the pre-industrial CO_2 level.

2. Additional information

Paleogeographic maps

The maps are derived from Golonka (2002). They have been digitized at a spatial resolution of 2.8° in longitude and 1.4° in latitude (Supplementary figure 8). The 5 maps correspond to the geographic configuration of the Tournaisian (350 Ma), the Mississippian-Pennsylvanian boundary (323 Ma), the Moscovian (308 Ma), the end of the Sakmarian (290 Ma), and the Cisuralian-Guadalupian boundary (272 Ma) (Supplementary figure 6). These maps have been used to define the outer shape (geographical extension) of the orogeny. To avoid an unrealistically sharp topographic break of several 1000 meters between the Hercynian Chain and the adjacent continental plains, the altitude on both sides of the Chain rises steady, in several steps as found in modern mountain ranges. Thus the highest altitudes are found mostly in the central parts of the Chain during the peak times of the orogeny.

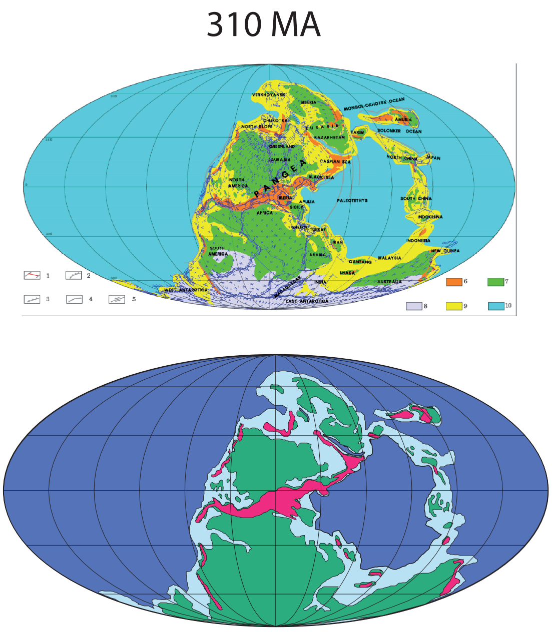

Supplementary figure 8: From original maps to numerical data. Upper panel shows the original map taken from Golonka (2002). Lower panel show paleogeography as used to build boundary conditions in FOAM. Note that the areal and extent of the Hercynian range (red shading on the lower panel) is directly taken from Golonka (2002). Our contribution has been to reconstruct altitude and slope for each time-slice.

The timing of the Hercynian orogeny is still a matter of debate. The Sudetic phase marking the definitive collision between Laurussia and Gondwana, occurs between 340 and 310 Ma (Veevers, 2013). The crustal scale elevator tectonics starts at 350-340 Ma (Dorr and Zulauf, 2010). The maximum altitude was probably reached around 320 Ma (Lardeaux et al., 2001). The Asturic phase (300 Ma) closes the orogenic cycles (Veevers, 2004). Aside from the timing, major uncertainties remain about the shape and altitude of the orogen. It could have been a Himalayan type mountain range (Rubatto et al., 2010; Kroner and Romer, 2013), a high altitude plateau (Becq-Giraudon et al., 1996), or a succession of narrow mountain ranges (Franke, 2014).

During the Tournaisian, we assume that the Hercynian orogenic phase was initiated, without distinctive relief (Supplementary Figure 6). The Hercynian range is only present on the four younger maps. Its maximum extension and altitude is reached during the Moscovian. We assume altitudes reaching 5000 m in the central section of the range (Becq-Giraudon et al., 1996; Fluteau et al., 2001). Then the altitude is decreasing with time: at 290 Ma, the maximum altitude is assumed to be 3000 m, and then falls to 2000 m at the end of the Cisuralian (Supplementary Figure 6).

The model does not include a spatial resolution of the lithology. We implicitly assume that each continental grid cell contains carbonate, shield rock and young volcanic rock outcrops (diffuse lithology).

Slopes in the past

For the five Paleozoic time slices, we define the slope of each grid cell from the present day correlation between slope and altitude (Supplementary figure 9). We add random noise to the calculated slopes. One possible bias of our simulations is the distribution of the altitudes on the continents: high altitudes and steep slopes are restricted to the reconstructed major mountain ranges, the remaining continental surface being flat (uniform altitude of 200 m). The present day distribution of altitude is indeed much more noisy. Our procedure, based on the altitude/slope correlation, is thus pending on the past prescribed altitudes. As a result, the reconstructed past continental surfaces are divided into two clearly distinct domains in terms of slopes.

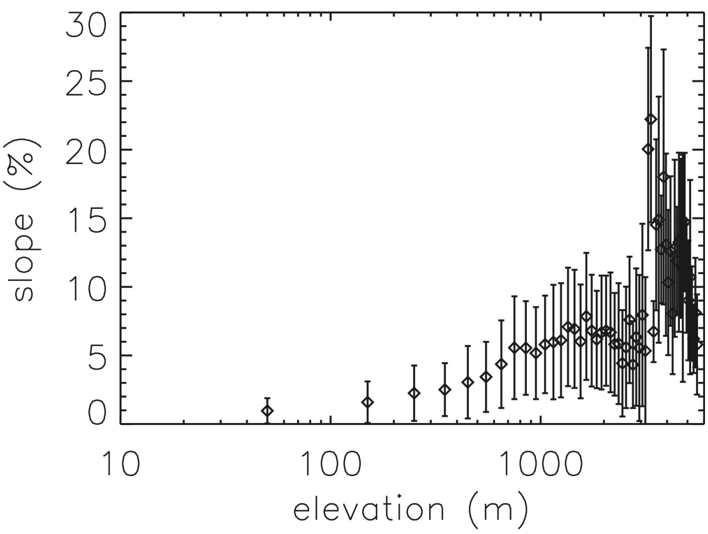

Supplementary figure 9: Relationship between the altitude (m) and the slope (%) for the present day world. The original data are extracted from SRTM (30" resolution).

In the present day correlation between slopes and altitudes, slopes are reaching their maximum values of about 20 % at 3000 m. Above 3000 m, slopes are declining to about 10 % (Supplementary figure 9). This feature is the imprint of the Tibetan high altitude plateau. In the GEOCLIM-REG simulation, we assume that the Hercynian orogeny is a Himalayan-type mountain range. Accordingly we keep the slopes around 20 % (with the additional random noise) even if the altitude of the Hercynian range exceeds 3000 m. An additional sensitivity run, which assumes that the range is a high altitude plateau, has been performed using the present day slope/altitude correlation (decreasing slopes above 3000 m). On Supplementary figure 10, we produce a map of the Himalayan slopes and of the relationship between slope and latitude for three 10° longitude-wide transects (data from Farr et al., 2007). The slopes can reach 30% at some locations but these are extreme values. Slopes are mostly oscillating between 5 and 15%. Mean values for these three transects are from 6 to 12 %. We then plot a 10° longitude-wide transect for the Hercynian range for each "slope" scenario, the Himalayan-like one and the plateau one. Slopes for the two mountain ranges are similar, showing that the Paleozoic slopes have not been overestimated. Mean values are 9.35 and 6.3 % for the two Paleozoic simulations, which are also within values found for the Himalayan orogeny.

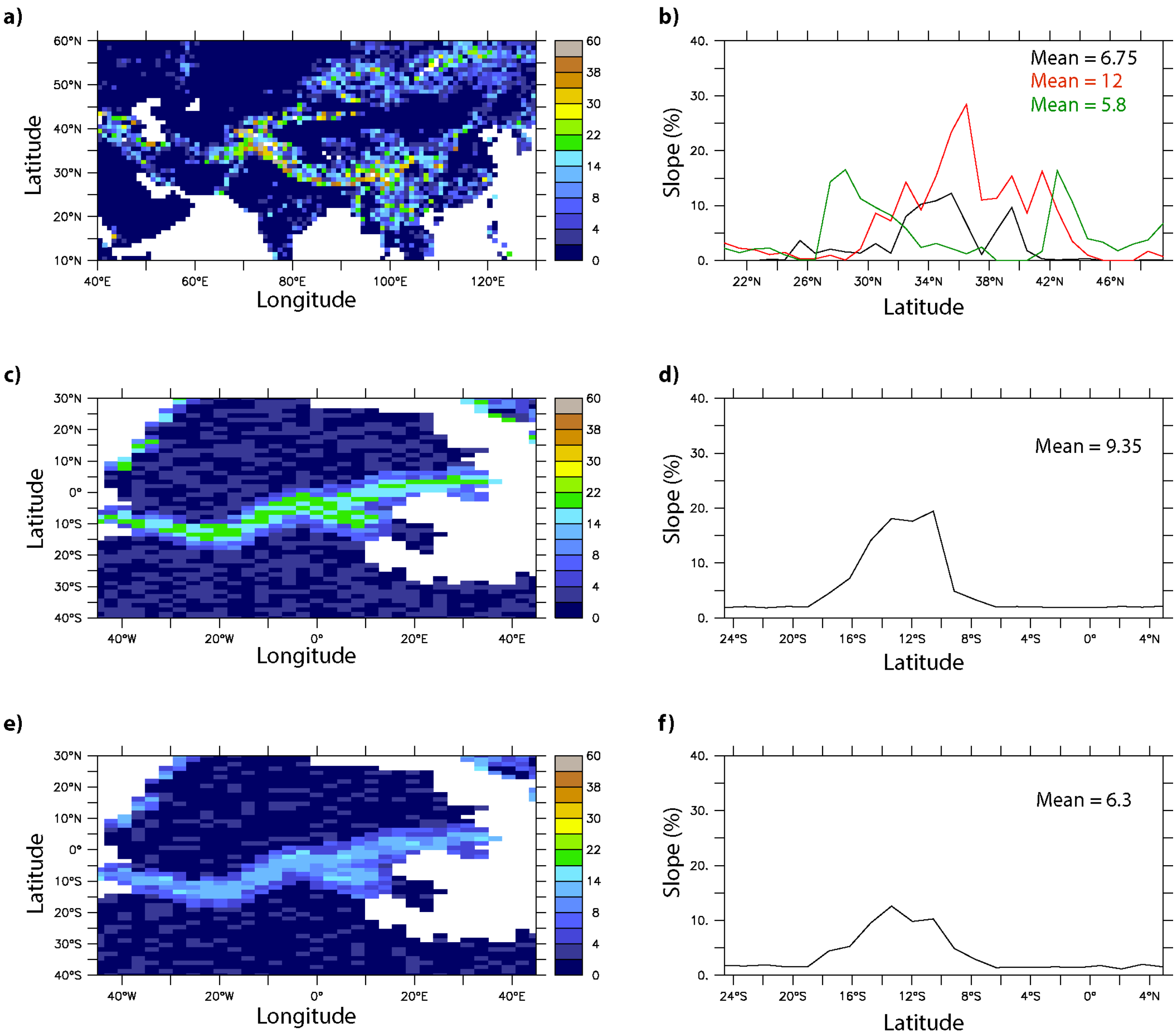

Supplementary figure 10: a) Actual slopes of the Himalayan region (SRTM DEM, Farr et al., 2007), c) Slopes of the Hercynian orogeny using the "Himalayan model" and c) Slopes of the Hercynian orogeny using a plateau-like range. b) Slope transects across the Himalayan ranges averaged over 10° longitude bands (black line = 60-70W; red line = 70W-80W and green line = 80W-90W). d) Slope transects across the Hercynian ranges averaged over 30W-20W. f) Same as d) but for the plateau scenario.

Starting CO_2 conditions at 350 Ma

Supplementary figure 11 shows that the CO_2 starting condition falls right in the middle of the range suggested by stomatal CO_2 proxies. In the GEOCLIM-REG simulations (Himalayan-type of mountain range), our model remains valid until the starting value stays below 2,500 ppmv (Supplementary figure 12). In the GEOCLIM-REG plateau simulations, a lower CO_2 starting value of 1,900 ppmv is required, which is still higher than the averaged CO_2 value as constrained by proxies (Supplementary figure 12).

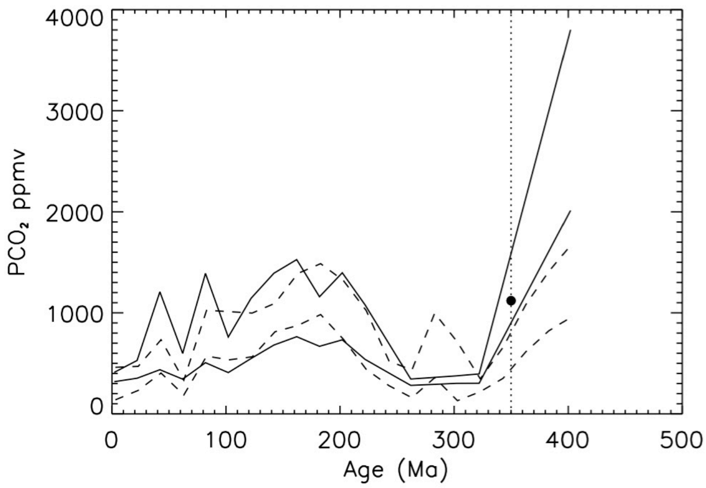

Supplementary figure 11: Proxy-based evolution of the atmospheric CO_2 level (Royer, personal communication, 2010). Solid lines: envelope containing 66 % of the CO_2 estimates based on stomatal index of fossil leaves. Dashed lines: envelope containing 66 % of the CO_2 estimates based on carbon isotopic compositions of pedogenic carbonates. The black dot stands for the initial value of CO_2 at 350 Ma (GEOCLIM, GEOCLIM-REG, GEOCLIM-WEST simulations).

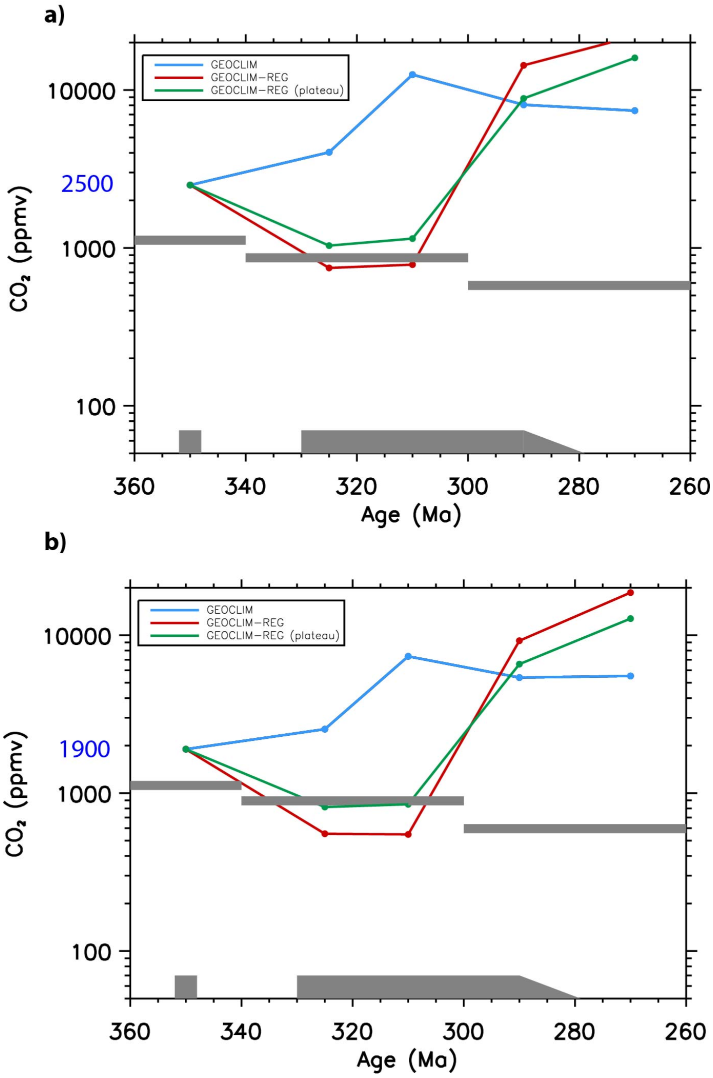

Supplementary figure 12: Calculated time evolution of the atmospheric CO_2 level for three simulations - a) for an initial CO_2 value of 2500 ppmv and b) for an initial CO_2 value of 1900 ppm.

The strontium isotopic model

The equation ruling the time evolution of the seawater $^{87}Sr/^{86}Sr$ (François and Walker, 1992) can be written as:

$$M_{oc}\frac{dr_{oc}}{dt} = \sum_{i=1}^{n} f_{sil}^{i}\alpha_{sil}\left(\frac{r_{sil}-r_{oc}}{9.43+r_{sil}}\right) + \sum_{i=1}^{n} f_{bas}^{i}\alpha_{bas}\left(\frac{r_{bas}-r_{oc}}{9.43+r_{bas}}\right) + f_{MOR}\alpha_{MOR}\left(\frac{r_{MOR}-r_{oc}}{9.43+r_{MOR}}\right) + \sum_{i=1}^{n} f_{carb}^{i}\alpha_{carb}\left(\frac{r_{carb}-r_{oc}}{9.43+r_{carb}}\right)$$

where M_{oc} is the total mass of Sr in the ocean and r_{oc} is the $^{87}Sr/^{86}Sr$ of seawater. n is the total number of continental grid cell. The f factors are the flux of carbon consumed by the weathering of basic rocks (*bas*), by the weathering of all other silicate lithologies (*sil*), by the weathering of carbonate rocks (*carb*). f_{MOR} is the release of CO_2 by mid-oceanic ridge systems

(*MOR*) (held constant for all time slices). The α factors are the proportionality constants between the carbon and strontium fluxes. r_{sil}, r_{bas}, r_{MOR} and r_{carb} are the associated $^{87}Sr/^{86}Sr$ ratios. The isotopic ratio of each source rock is assumed to be the same for each continental grid cell. Assuming steady state (residence time of Sr in seawater is about 2 million years, largely below the time resolution of the present study), we set the derivative term of the equation to zero and solve it for r_{oc}.

r_{carb} is assumed to be close to the average value of the seawater $^{87}Sr/^{86}Sr$ prior to the period of study, and is accordingly fixed at 0.708 (Veizer et al., 1999). The other isotopic ratios *r* are calculated as follows (Vidal, 1994):

$$r_{MOR} = BABI + \left(\frac{^{87}Rb}{^{86}Sr}\right)_m \left(1 - e^{-\lambda t}\right)$$

where *t* is the age of the considered time slice, with t=0 at the origin of the Earth (age of the Earth fixed at 4.54×10^9 years). *BABI* is the Basaltic Achondrite Best Initial ratio and λ is the ^{87}Rb decay constant. $(^{87}Rb/^{86}Sr)_m$ is the $^{87}Rb/^{86}Sr$ of the mantle. r_{bas} is set equal to r_{MOR}, implicitly assuming that young basaltic rocks have the $^{87}Sr/^{86}Sr$ of the mantle at the age of the considered time slice. Finally, the $^{87}Sr/^{86}Sr$ of other silicate rocks is calculated as the $^{87}Sr/^{86}Sr$ of continental rocks differentiated from the mantle about 2.5 byr ago:

$$r_{sil} = BABI + \left(\frac{^{87}Rb}{^{86}Sr}\right)_m \left(1 - e^{-\lambda \cdot 2 \cdot 10^9}\right) + \left(\frac{^{87}Rb}{^{86}Sr}\right)_{CC} \left(1 - e^{-\lambda\left(t - 2 \cdot 10^9\right)}\right)$$

$(^{87}Rb/^{86}Sr)_{CC}$ is the $^{87}Rb/^{86}Sr$ of the continental crust. This value is about 10 times bigger than the corresponding mantle value (Vidal, 1994). We used it as a calibration constant so that the $^{87}Sr/^{86}Sr$ of seawater equals 0.7092 under present day climatic conditions (control run). The following table gives the values of the parameters.

Parameters of the strontium isotopic budget

Parameter	Symbol	value	units	Reference
Carbonate rock $^{87}Sr/^{86}Sr$	r_{cw}	0.708	-	Veizer et al. (1999)
BABI	BABI	0.69897	-	Vidal (1994)
Mantle Rb/Sr	$RbSr_m$	0.025	-	Vidal (1994)
Mantle $^{87}Rb/^{86}Sr$	$(^{87}Rb/^{86}Sr)_m$	0.0699	-	Vidal (1994)
Continental crust Rb/Sr	$(^{87}Rb/^{86}Sr)_{CC}$	0.1746	-	calibrated
^{87}Rb decay constant	λ	1.42×10^{-11}	yr^{-1}	Vidal (1994)
Mean age for the differentiation of the continental crust	T_c	2.5×10^9	yr	Vidal (1994)
Sr/C flux ratio for the weathering of basaltic rocks	α_{bas}	0.00375	-	Wallman (2001)
Sr/C flux ratio for the weathering Of other silicate rocks	α_{sil}	0.0027	-	Wallman (2001)
Sr/C flux ratio at MOR	α_{MOR}	0.00475	-	Wallman (2001)
Sr/C flux ratio for the weathering Of continental carbonates	α_{carb}	0.00035	-	Wallman (2001)

Spatial distribution of the shielding factor

Supplementary figure 13 displays the $\log_{10}$ of the shielding factor for each time slice (GEOCLIM-REG simulation) under a constant CO_2 of 4 times the pre-industrial level (1120 ppm). From the top to the bottom: 350 Ma, 323 Ma, 308 Ma, 290 Ma and 272 Ma The shielding factor is arbitrarily set to 1 for regions where the calculated runoff is equal to 0 (those regions do not contribute to the global weathering flux). Comparing the maps at 350 Ma and 308 Ma, the shielding factor increases by 1 to 2 orders of magnitude in the equatorial area, due to the rise of the Hercynian mountain range.

(a)

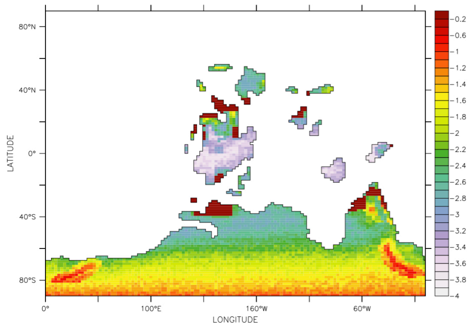

(b)

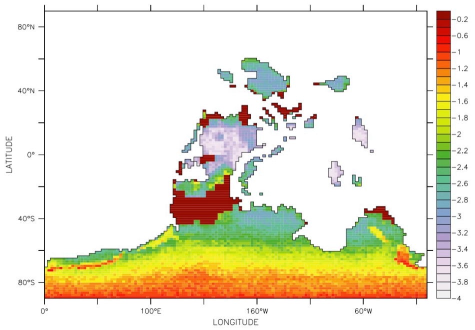

(c)

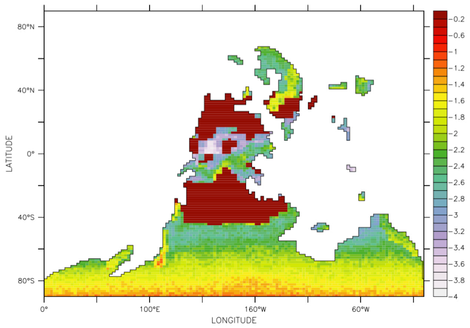

(d)

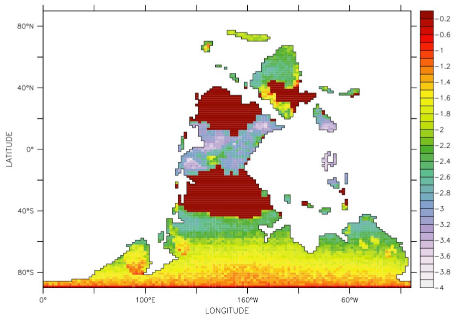

(e)

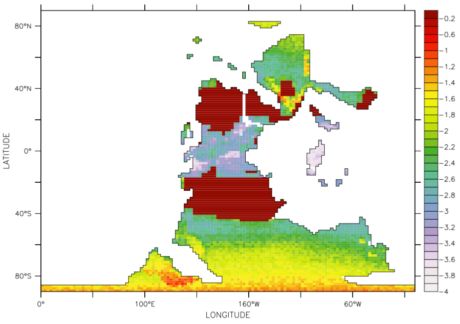

Atmospheric CO_2

The model-proxies CO_2 comparison shows a nice fit for Carboniferous times but a divergence between proxies and our model occurs for Permian times, the model calculating CO_2 largely above the 1σ-envelop of the available proxies. Two sets of proxies are available for the Carboniferous and Permian: one based on the stomatal index of fossil leaves, and the other on the $\delta^{13}C$ of pedogenic carbonates from paleosols. The stomatal method is well known for its lack of precision for CO_2 levels above 1,000 ppm. The calibration of stomata proxy at high CO_2 is weakly constrained (Beerling and Royer, 2002; Beerling et al., 2009) and recent evidence that leaves adapt the size of the stomata and in addition their density at high CO_2 values (Franks and Beerling, 2009) raises questions about the validity of the stomatal proxy at high CO_2. Smith et al. (2010) recently affirmed that the stomatal methods should probably be considered semi-quantitative under high CO_2 conditions and may represent CO_2 minima. As noted by Huber and Caballero (2011), « *existing proxy records have much greater accuracy at low CO_2 and once values are significantly higher than modern (somewhere above 560 to 1220 ppm, depending on the proxy), there is little certainty in the actual value* ». Regarding the paleosol proxy, the critical parameter is the amount of CO_2 respired in the soil. This parameter is fit on present day field measurements (Breecker et al., 2010), and then exported in the past. Its reliability probably decreases with increasing age, since biomes are increasingly different from the present day biomes. This said, the general temporal trends defined by proxy data are probably more reliable than absolute values. Our model simulations (GEOCLIM-REG and GEOCLIM-West) are in agreement with those trends.

Nevertheless, modeled CO_2 levels depend on the sensitivity of the climate model to a CO_2 doubling. The atmospheric component of FOAM originates from the NCAR model, which has a relatively weak sensitivity of global mean temperature to increased greenhouse gas concentrations (2– 3 ◦C warming for doubling of atmospheric CO_2 levels). This sensitivity is at the lower end of the IPCC range. Doubling the climatic sensitivity in our model (see next section) does not alter our scenario but considerably reduces atmospheric CO_2 levels during Permian times (9 to 14 X).

Climate sensitivity

We describe here the procedure we apply to modify the climate sensitivity of the FOAM GCM. For each time slice and for each grid element *i*, we calculate a regression line (slope l_i and ordinate at origin B_i) fitting the annual temperature T_i calculated by the FOAM GCM as a function of the logarithm of the atmospheric CO_2 partial pressure.

$$T_i = l_i \cdot log(PCO_2) + B_i$$

The slope of each line l_i is then multiplied by 2 and the new temperatures of each grid element are recalculated for each CO_2 level and for each time slice. The new runoff of each grid element is modified using the regression lines of runoff vs mean annual temperature calculated for each continental grid element from the FOAM GCM runs.

Climatology

The calculated runoff and air temperature at the surface corresponding to the calculated steady state atmospheric CO_2 (GEOCLIM-REG simulation) for each time slice can be downloaded at the following address:

https://geoclimmodel.wordpress.com/download-area/

The following table provides the atmospheric CO_2 for each time slice.

Age (Ma)	Steady state atmospheric CO_2 (ppm) (GEOCLIM_REG simulation)
350	1148
323	339
308	336
290	5320
272	13160

Graphical representation of the CO_2 calculation method

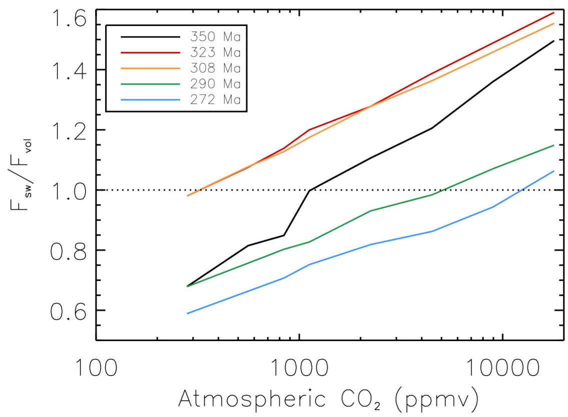

Supplementary figure 14: graphical representation of the method used to calculate the atmospheric CO_2 (GEOCLIM-REG case). Each curve represents the global CO_2 consumption by continental silicate weathering (sum of the contribution of each grid element) divided by the total solid Earth degassing (prescribed), as a function of atmospheric CO_2. Steady state CO_2 is reached when the silicate weathering/CO_2 degassing ratio equals 1.

Supplementary table 1: model parameters

Parameter	Numerical value	Units	Reference	Model
k_G^{CO2}	$4.35\ 10^{-4}$	mol/m³	Calibration	GEOCLIM GEOCLIM-REG
$k_{G,b}^{CO2}$	$6.46\ 10^{-5}$	mol/m³	Calibration	GEOCLIM GEOCLIM-REG
E_a	48200	J/mol	Oliva et al.(2003)	GEOCLIM GEOCLIM-REG
$E_{a,b}$	42300	J/mol	Dessert et al. (2003)	GEOCLIM GEOCLIM-REG
k_d	$4\ 10^{-4}$		Calibration	GEOCLIM-REG
k_a	$2.8\ 10^{2}$		Calibration	GEOCLIM-REG
k_1	0.8		Carretier et al. (2014)	GEOCLIM-REG
d_1	0.5	m	Carretier et al. (2014)	GEOCLIM-REG
d_2	0.1	m	Carretier et al. (2014)	GEOCLIM-REG
ρ	8.314	J/(mol K)	Ideal gas constant	GEOCLIM GEOCLIM-REG
k_{Gr}^{CO2}	$7.23\ 10^{2}$	mol/m³	Calibration	GEOCLIM-REG
K	$2.6\ 10^{-4}$		West (2012)	GEOCLIM-REGw
k_w	$7.6\ 10^{-5}$		West (2012)	GEOCLIM-REGw
E_a	14600	J/mol	West (2012)	GEOCLIM-REGw
z	41	t/m²	West (2012)	GEOCLIM-REGw
$\sigma+1$	1.13		West (2012)	GEOCLIM-REGw
k_{Grw}^{CO2}	$2.15\ 10^{15}$		Calibration	GEOCLIM-REGw

References

Becq-Giraudon, J.-F., Montenat, C. & Van Den Driessche, J. Hercynian high-altitude phenomena in the French Massif Central: tectonic implications. *Palaeogeogr. Palaeoclim. Palaeoecol.* **122**, 277-241 (1996).

Beerling, D. J. and Royer, D. L.: Reading a CO2 signal from fossil stomata, New Phytol., 153, 387–397, 2002

Beerling, D. J., Fox, A., and Anderson, C. W.: Quantitative uncertainty analyses of ancient atmospheric CO2 estimates from fossil leaves, Am. J. Sci., 309, 775–787, doi:10.2475/09.2009.01, 2009

Breecker, D.O., Sharp, Z.D., and McFadden, L.D. : Atmospheric CO2 concentrations during ancient greenhouse climates were similar to those predicted for A.D. 2100. Proc. Nat. Acad. Sci., 107, 576-580, 2010.

Carretier, S., Goddéris, Y., Delannoy, T. & Rouby, D. Mean bedrock-to-saprolite conversion and erosion rates during mountain growth and decline. *Geomorphology* **209**, 39-52 (2014).

Dessert, C., Dupré, B., Gaillardet, J., François, L. M. & Allègre, C. J. Basalt weathering laws and the impact of basalt weathering on the global carbon cycle. *Chemical Geology* **202**, 257-273 (2003).

Dörr, W. & Zulauf, G. Elevator tectonics and orogenic collapse of a Tibetan-style plateau in the European Variscides: the role of the Bohemian shear zone. *Int. J. Earth Sci.* **99**, 299-325 (2010).

Farr, T.G., Rosen, P.A., Caro, E., Crippen, R., Duren, R., Hensley, S., Kobrick, M., Paller, M., Rodriguez, E., Roth, L., Seal, D., Shaffer, S., Shimada, J., Umland, J., Werner, M., Oskin, M., Burbank, D. & Alsdorf, D. The shuttle radar topography mission. Rev. Geophys., 45, RG2004, doi: 10.1029/2005RG000183 (2007).

Fluteau, F., Besse, J., Broutin, J. & Ramstein, G. The Late Permian climate. What can be inferred from climate modelling concerning Pangea scenarios and Hercynian range altitude? *Palaeogeogr. Palaeoclim. Palaeoecol.* **167**, 39-71 (2001).

François, L.M. & Walker, J.C.G. Modelling the Phanerozoic carbon cycle and climate: constraints from the $^{87}Sr/^{86}Sr$ isotopic ratio of seawater. *Am. J. Sci.* **292**, 81-135 (1992)

Franke, W. Topography of the Variscan orogeny in Europe: failed – not collapsed. *Int. J. Earth Sci.* **103**, 1471-1499 (2014).

Franks, P. J. and Beerling, D. J.: Maximum leaf conductance driven by CO2 effects on stomatal size and density over geologic time, P. Natl. Acad. Sci. USA, 106, 10 343–10 347, doi:10.1073/pnas.0904209106, 2009

Gaillardet, J., Dupré, B., Louvat, P. & Allègre, C. J. Global silicate weathering and CO_2 consumption rates deduced from the chemistry of the large rivers. *Chemical Geology* **159**, 3-30 (1999).

Galy, A. & France-Lanord, C. Weathering processes in the Ganges-Brahmaputra basin and the riverine alkalinity budget. *Chemical Geology* **159**, 31-60 (1999).

Golonka, J. Plate-tectonic maps of the Phanerozoic, in Kiessling, W., Flügel, E., Golonka, J. (eds) *Phanerozoic Reef Patterns*, SEPM Special Publications **72**, 21-75 (2002).
Heimsath, A. M., Hancock, G. R. & Fink, D. The 'humped' soil production function: Eroding Arnhem Land, Australia. *Earth Surface Processes and Landforms* **34**, 1674-1684 (2009).

Kroner, U. & Romer, R. L. Two plates – many subduction zones: the Variscan orogeny reconsidered. *Gondwana Res.* **24**, 298-329 (2013).

Laraque, A. *et al.* A comparison of the suspended and dissolved matter dynamics of two large inter-tropical rivers draining into the Atlantic Ocean: the Congo and the Orinoco. *Hydrological Processes* **27**, doi:10.1002/hyp.9776 (2013).

Lardeaux, J. M., Ledru, P., Daniel, I. & Duchene, S. The Variscan French Massif Central – a new addition to the ultra-high pressure metamorphic 'club': exhumation processes and geodynamic consequences. *Tectonophysics* **332**, 143-167 (2001).

Ludwig, W. & Probst, J.-L. River sediment discharge to the oceans: present-day controls and global budget. *American Journal of Science* **298**, 265-295 (1998).

Meybeck, M., Matti, K. & Dürr, H. Global hydrobelts and hydroregions: improved reporting scale for water-related issues? *Hydrology and Earth System Sciences* **17**, 1093-1111, doi:10.5194/hess-17-1093-2013 (2013).

Milliman, J. D. & Syvitski, P. M. Geomorphic/tectonic control of sediment discharge to the ocean: importance of small mountainous rivers. *Journal of Geology* **100**, 524-544 (1992).

Millot, R., Gaillardet, J., Dupré, B. & Allègre, C. J. The global control of silicate weathering rates and the coupling with physical erosion: new insights from rivers of the Canadian Shield. *Earth and Planetary Science Letters* **196**, 83-98 (2002).

Rubatto, D., Ferrando, S., Compagnoni, R. & Lombardo, B. Carboniferous high-pressure metamorphism of Ordovician protoliths in the Argentera Massif (Italy), southern European Variscan belt. *Lithos* **116**, 65-76 (2010).

Smith, R. Y., Basinger, J. F., and Greenwood, D. R.: Depositional setting, fossil flora, and paleoenvironment of the Early Eocene Falkland site, Okanagan Highlands, British Columbia, Can. J. Earth Sci., 46, 811–822, doi:10.1139/E09-053, 2009

Veevers, J. J. Gondwanaland from 650-500 Ma assembly through 320 Ma merger in Pangea to 185-100 Ma breakup: supercontinental tectonics via stratigraphy and radiometric dating. *Earth-Sci. Rev.* **68**, 1-132 (2004).

Veevers, J. J. Pangea: geochronological correlation of successive environmental and strati-tectonic phases in Europe and Australia. *Earth-Sci. Rev* **127**, 48-95 (2013).

Veizer, J., Ala, D., Azmy, K., et al. $^{87}Sr/^{86}Sr$, $\delta^{13}C$ and $\delta^{18}O$ evolution of Phanerozoic seawater. *Chem. Geol.* **161**, 59-88 (1999).

Vidal, P. Géochimie, Dunod, 190 p., Paris (1994).

Wallmann, K. Controls on the Cretaceous and Cenozoic evolution of seawater composition, atmospheric CO_2 and climate. Geochim. Cosmochim. Acta **65**, 3005-3025 (2001).